Article

Control of Positive and Negative Magnetoresistance in Iron Oxide–Iron Nanocomposite Thin Films for Tunable Magnetoelectric Nanodevices

Martin Nichterwitz, Shashank Honnali, Jonas Zehner, Sebastian Schneider, Darius Pohl, Sandra Schiemenz, Sebastian T. B. Goennenwein, Kornelius Nielsch, and Karin Leistner*

Cite This: *ACS Appl. Electron. Mater.* 2020, 2, 2543–2549

Read Online

ACCESS | Metrics & More | Article Recommendations | Supporting Information

ABSTRACT: The perspective of energy-efficient and tunable functional magnetic nanostructures has triggered research efforts in the fields of voltage control of magnetism and spintronics. We investigate the magnetotransport properties of nanocomposite iron oxide/iron thin films with a nominal iron thickness of 5−50 nm and find a positive magnetoresistance at small thicknesses. The highest magnetoresistance was found for 30 nm Fe with +1.1% at 3 T. This anomalous behavior is attributed to the presence of Fe_3O_4−Fe nanocomposite regions due to grain boundary oxidation. At the Fe_3O_4/Fe interfaces, spin-polarized electrons in the magnetite can be scattered and reoriented. A crossover to negative magnetoresistance (−0.11%) is achieved at a larger thickness (>40 nm) when interface scattering effects become negligible as more current flows through the iron layer. Electrolytic gating of this system induces voltage-triggered redox reactions in the Fe_3O_4 regions and thereby enables voltage-tuning of the magnetoresistance with the locally oxidized regions as the active tuning elements. In the low-magnetic-field region (<1 T), a crossover from positive to negative magnetoresistance is achieved by a voltage change of only 1.72 V. At 3 T, a relative change of magnetoresistance about −45% during reduction was achieved for the 30 nm Fe sample. The present low-voltage approach signifies a step forward to practical and tunable room-temperature magnetoresistance-based nanodevices, which can boost the development of nanoscale and energy-efficient magnetic field sensors with high sensitivity, magnetic memories, and magnetoelectric devices in general.

KEYWORDS: *magnetoresistance, voltage control of magnetism, magneto-ionic control, magnetite, iron films*
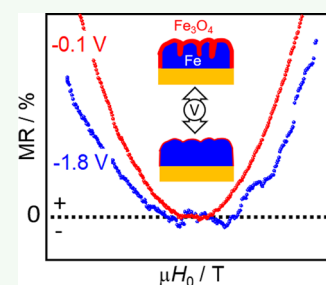
INTRODUCTION

The understanding and control over magnetoresistance (MR) in nanostructured materials is crucial for the development of modern magnetic sensors,[1,2] high-density information storage,[3] spintronics,[4,5] biochips,[6] magnetoelectronic logic devices[7] or microwave nanoelectronics.[8] Intense research efforts have been focussed on tailoring MR by optimizing the material composition and nanostructure, and, ideally, finding systems in which MR is tunable by an external control parameter, *e.g.*, by electric fields or optical modulation.[9,10] In semiconductor nanowires[11−13] and spin-valve devices,[14] as well as atomically thin Weyl semimetals,[15] large changes of MR by electric field effects have been demonstrated. However, in these cases, the tunable MR becomes significant only at low temperatures (<5 K) or the synthesis routes are complex. Voltage control of magnetic layers is another promising route to control MR. For example, voltage-tunable giant magnetoresistance (GMR) and tunneling magnetoresistance (TMR) have been achieved via capacitive electronic charging induced changes of magnetic anisotropy[16] or multiferroic effects[17] in ferromagnetic layers. Here, high electric fields or strain coupling in complex layer architectures are required to achieve large effects.

Interfacial electrochemical effects on magnetism,[18] often also named magneto-ionic effects,[19] are an emerging room-temperature and low-voltage approaches in the research area of voltage control of magnetism.[20,21] In magneto-ionic systems, the magnetic layer is gated via a solid or liquid electrolyte and the voltage triggers ion migration and interfacial redox reactions, which impact the magnetic properties. In contrast to multiferroic systems and capacitive electronic charging, magneto-ionic concepts make significant magnetic property changes possible at room temperature and without the need for strain mediation. A magneto-ionic control of magnetization, exchange bias, and coercivity is well documented in various ferromagnetic metal/metal oxide systems.[19,22−25] A tunable negative magnetoresistance was achieved in a Fe_3O_4 thin film using the mechanism of Li^+ ion insertion and removal.[26]
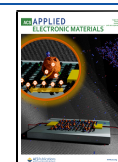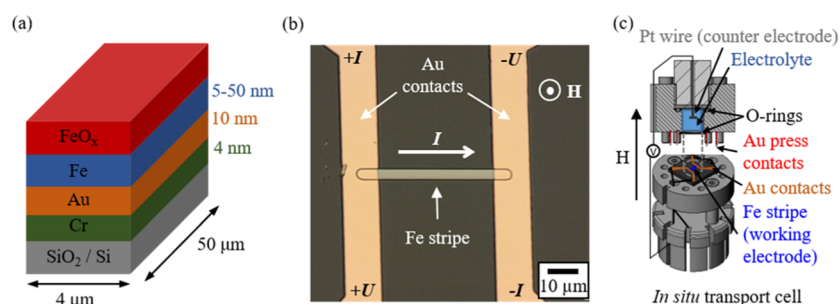
Figure 1. (a) Layer architecture of the iron oxide/iron thin film stripe. (b) Light microscopy image of an iron oxide/iron stripe with Au contacts for the MR measurement. The directions of magnetic field H, applied current I, and measured voltage U are indicated. (c) Sketch of the *in situ* transport cell for the MR measurements, with the iron oxide/iron stripe as the working electrode and a Pt wire as the counter electrode immersed in the electrolyte.

In the present study, we produced Fe_3O_4/iron films in stripe geometry by lithography and sputtering followed by native oxidation. Their magnetoresistance was investigated ex situ and during electrolytic gating at room temperature. We demonstrate tunable sign and magnitude of MR at room temperature by tailoring the film thickness and exploiting magneto-ionic control in the iron oxide—iron nanocomposite thin films. The effects are attributed to a variety of spin scattering at Fe_3O_4/iron interfaces.

EXPERIMENTAL SECTION

Device Fabrication. The devices for transport measurements were prepared on thermally oxidized (100 nm) Si (100) wafer substrates (1 cm × 1 cm) as follows: First, contact pads consisting of Au (100 nm)/Cr (5 nm) layers were deposited by DC magnetron sputtering (1.2×10^{-6} mbar, room temperature, Ar sputtering gas) in the substrate corners using a shadow mask. Second, different stacks with varying nominal Fe layer thickness ($d_{Fe,nom}$) [Fe($d_{Fe,nom}$ = 5−50 nm)/ Au (10 nm)/ Cr (4 nm)] in stripe geometry (4 μm x 50 μm nominal lateral dimensions, see Figure 1a) were produced on the substrate by lithography steps, followed by DC magnetron sputtering (2×10^{-8} mbar, room temperature, Ar with 2% H_2 sputtering gas). For comparison, stacks of [Au (10 nm)/ Fe (30 nm)/ Au (10 nm)/ Cr(4 nm)], [Fe (30 nm)], and [Fe (30 nm)/ Pd(10 nm)/ Cr (4 nm)] were prepared in stripe geometry in the same manner. During this step, the gold, iron, and palladium target guns had an inclination angle of 45° with respect to the substrate normal. The stripes were then removed from the sputtering chamber to ambient air condition, which causes the formation of a native iron oxide layer on top of the sputtered Fe. Note that the passivating iron oxide layer on the nanocrystalline iron films forms within few minutes and remains stable during the subsequent storage at room temperature and in dry (lab) atmosphere.[27−29] Third, a second lithography step and subsequent sputtering, under the same conditions as step 1, was performed to form Au/Cr contacts between the stripe edges and the contact pads. To avoid Schottky barrier contacts and remove the iron oxide layer from the iron stripe at the contact points, Ar plasma etching was performed prior to Au/Cr deposition.

Microstructural Characterization. High-resolution transmission electron microscopy (HR-TEM) was conducted on a double-aberration-corrected Thermo Fisher Scientific Titan[3] 80-300 microscope to investigate the film layer architecture and microstructure. The preparation of the cross-section lamella was carried out via a focused ion beam technique in a Thermo Fisher Scientific Helios Nanolab 600i with 30 and 4 kV Ga^+ ions. Further thinning of the lamella was performed in a Gatan PIPSII with 0.2 kV Ar^+ ions. Fast Fourier transformations (FFTs) were performed for selected sample areas using the Gatan Microscopy Suite. Scanning transmission electron microscopy and energy-dispersive X-ray diffraction (STEM-EDX) measurements were conducted in a JEOL Jem F-200C microscope operated at 200 kV. The convergence angle was set to

10 mrad. Raman spectra were recorded using a 532 nm excitation wavelength of a Torus 532 laser (Laser Quantum) on a T64000 triple spectrometer (Jobin Yvon) Horiba, equipped with a diffraction grid of 600 gr/mm. The laser power was adjusted to less than 7.3 μW to avoid laser-induced iron oxide transformation[30] (see Supporting Information S1). The laser spot on the sample had a diameter of 20 μm. The spectra were obtained with an acquisition time of 150 s, accumulated five times.

***In Situ* Magnetoresistance Measurements.** The MR measurements were performed in a physical property measurement system magnetometer (PPMS6100, Quantum Design). The samples were measured within a few weeks after preparation. A current of 10 μA was applied in-plane along the stripe and the corresponding voltage was detected (Figure 1b). A magnetic field $\mu_0 H$ of up to ±3 T was applied perpendicular to the substrate plane at a rate of 20 mT s^{-1}. The MR curves were corrected using a linear fit for each field sweep (+3 to −3 T and −3 to +3 T), followed by symmetrization. All MR measurements were performed in a custom-built electrochemical cell shown in Figure 1c and described in detail in previous work.[31] First, an *ex situ* MR measurement without electrolyte was performed. The behavior of the stripes upon sole contact with the electrolyte was then probed by an *in situ* MR measurement. For this, the electrolyte compartment was filled with 1 mol/L LiOH aqueous solution and no external voltage was applied, corresponding to the open-circuit potential (OCP) state. A Pt wire, placed in the electrolyte, served as the counter electrode to apply the reduction and oxidation potentials (E_{Red}, E_{Ox}) via an additional external Keithley 2400 sourcemeter. MR measurements were then performed at specific potentials. The potentials for reduction to metallic iron and reoxidation to iron oxide were chosen on the basis of the previously conducted three-electrode measurements as E_{Red} = −1.84 V and E_{Ox} = −0.12 V, respectively.[32] During the reduction step, the iron oxide/iron stripe is the cathode, while during the oxidation step it is the anode. To minimize the dissolution processes, the potential is switched, and not ramped, between the oxidation and the reduction step.[33]

RESULTS AND DISCUSSION

To search for tunable magnetotransport properties, we chose iron oxide/iron films with different nominal thicknesses on an Au buffer layer, which are suitable for magneto-ionic control.[32] Au is utilized as an underlayer to ensure sufficient electrical conductivity of the working electrode during electrolytic gating. Since in the present stripe geometry, the buffer layer is in contact with the electrolyte at the vertical edges, it must also be inert with regard to the electrochemical processes. Au is preferred over Pd or Pt here because, in contrast to those metals, it does not catalyze the hydrogen evolution reaction, which can lead to undesired pH changes or gas bubbling during the reduction process in the electrolyte.[22,34]

The native iron oxide layer forms on top of the iron film when removing the sample from the sputter chamber. To

characterize the nanostructure and type of iron oxide, HR-TEM and Raman spectroscopy were conducted. Figure 2a
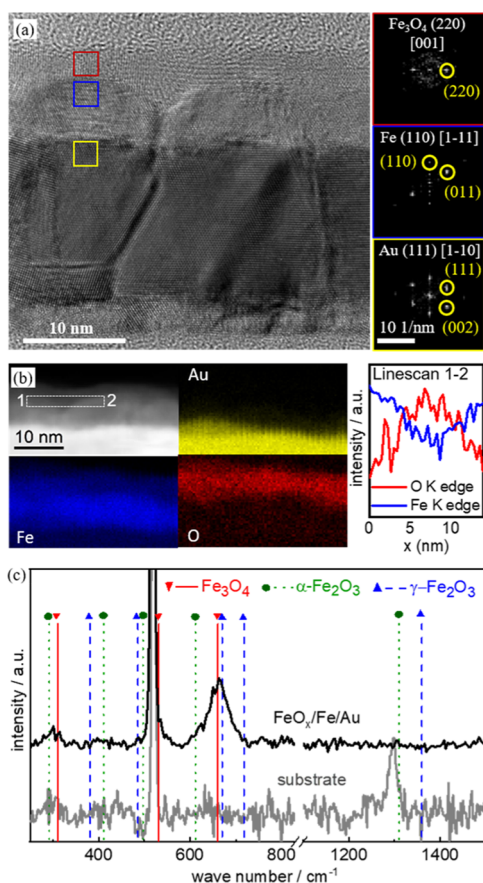
Figure 2. Composition and morphology of pristine iron oxide−iron nanocomposite films. (a) Cross-sectional HR-TEM image and FFTs of a FeO_x/Fe/Au/Cr layer stack show nanosized iron grains covered by the native iron oxide layer. (b) Cross-sectional STEM image with associated EDX maps for Au (L-edge), Fe, and O (K-edges) and a line scan over these maps showing the enhanced oxygen content in the dent between two iron grains. (c) Raman spectrum identifies Fe_3O_4 as the dominant native oxide.

shows the HR-TEM image of a film with $d_{Fe,nom}$ of 10 nm after the native oxidation. Iron grains with lateral dimensions in the range of 10 nm are observed, which are covered by an ∼3 nm thin iron oxide layer. At the grain boundaries, due to the curvature of the iron grains, the iron oxide penetrates deeper into the iron layer. This is evidenced further by the STEM-EDX investigations. The associated EDX mappings for oxygen (O−K) and iron (Fe−K), and a line scan over these EDX elemental maps show an enhanced oxygen content in the dent between two iron grains (Figure 2b). Raman measurements (Figure 2c) show only modes for magnetite (Fe_3O_4) besides the substrate peak. Since no peaks for the hematite and maghemite, and no peak splitting of the A_{1g} phonon mode 661 cm^{-1}, are detected, Fe_3O_4 is confirmed as the dominant iron oxide,[35−37] even though small amounts of other iron oxides cannot be fully excluded (see Supporting Information S1). The formation of a crystalline magnetite layer is expected for native oxidation of iron in ambient conditions[29,38−40] and consistent with the fast Fourier transform (FFT) of the HR-TEM image (Figure 2a) in the iron oxide region of the sample. X-ray diffraction resolves a broad Fe(110) peak for this sample,

reflecting the nanocrystalline nature of the thin film (see Supporting Information S2). It can be concluded that, for small enough thicknesses, the natively oxidized iron thin films can be regarded as iron oxide−iron nanocomposite films with nanosized iron grains embedded in a Fe_3O_4 layer.

The deposition of films with different sputtered nominal iron thickness and subsequent native oxidation is a route to prepare films with different iron oxide/iron metal ratios. The reason is that the thickness of the native oxide layer at the iron surface is expected to be approximately constant and independent of the underlying iron thickness.[41] The larger the nominal deposited iron film thickness, the smaller is the surface-to-volume ratio; this directly results in a decreased oxide-to-metal ratio after native oxidation. The previous reports[40] on the native oxidation of sputtered Fe films show that this effect is amplified by thickness-dependent morphological features. The transition from an island-like to a film-like growth mode will cause a further decrease of the surface area at increasing film thickness.[22] In addition, after coalescence of the nanoislands, the film thickness increase will lead to a deeper extension of the vertical grain boundaries in the film, which makes them less susceptible to grain boundary oxidation. All three effects occur in the present iron films and will result in an especially large iron oxide/metal ratio at small film thickness.

The MR of the iron oxide−iron nanocomposites was investigated for samples with a different sputtered nominal iron thickness between 5 and 50 nm and compared to the MR of the substrate and a pure iron stripe. The MR is defined as $[R(H) - R(0)]/R(0)$, where R is the resistance, H is the external magnetic field, and $R(0)$ is the resistance at zero magnetic field. Figure 3a shows the MR curves for the sole Au/Cr buffer layer and a 30 nm thick iron stripe protected from oxidation by an Au cover layer. The Au/Cr stripe sample showed a small positive MR, which is as expected for Au exhibiting the ordinary magnetoresistance effect (OMR).[42] For the sandwiched pure iron stripe, a small negative MR is observed. The measurable negative MR effect is small and rather noisy because most of the current flows through the top and bottom Au layers, which are more conductive than iron. This negative MR is as expected for ferromagnetic layers, when measuring in the transverse current−magnetic field geometry, and can be explained by spin−orbit coupling.[43] In contrast to this, Figure 3b shows that a positive MR occurs when the iron stripes with $d_{Fe,nom}$ = 30 nm are natively oxidized. Large positive MR values of 1.1 and 1.5% at 3 T are obtained with and without Au/Cr buffer layer, respectively. In Figure 3c, the MR curves for films with 5 nm ≤ $d_{Fe,nom}$ ≤ 50 nm on an Au/Cr buffer layer are plotted. The MR at $\mu_0 H$ = 3 T extracted from these curves is plotted in Figure 3d in depending on $d_{Fe,nom}$. For the iron oxide−iron nanocomposite films, the increase of $d_{Fe,nom}$ from 5 to 30 nm leads to an increasingly positive MR up to a maximum of +1.1% at $d_{Fe,nom}$ of 30 nm. For thicknesses of $d_{Fe,nom}$ > 30 nm, MR decreases again and finally changes sign from positive to negative at $d_{Fe,nom}$ ≥40 nm. This negative MR at large iron layer thickness is expected for ferromagnetic layers. The positive MR observed at the lower thickness, however, is rather unusual for room-temperature measurements.

This distinct thickness dependence of MR and the positive MR at room temperature are discussed in the following by taking into account the nanocomposite Fe_3O_4−Fe microstructure of the films. For both Fe and Fe_3O_4, a negative MR is expected and usually observed.[44−49] There are, however, also
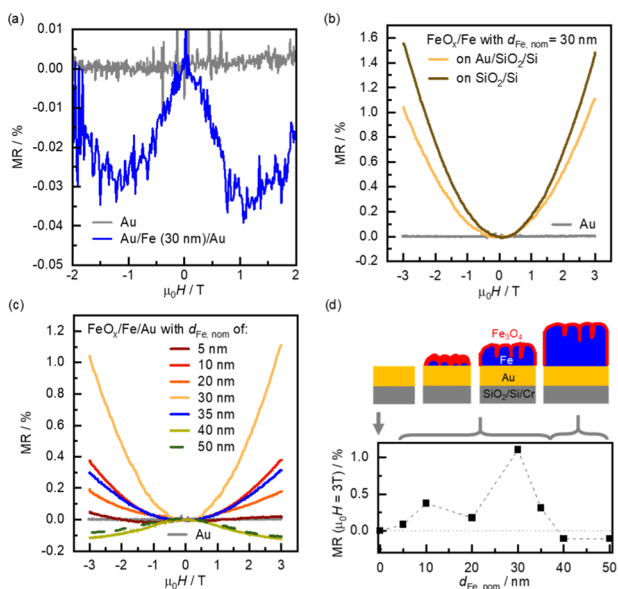
Figure 3. (a–c) MR of (a) an iron stripe protected by an Au (10 nm) top layer, (b) iron oxide–iron nanocomposite stripes with and without Au/Cr underlayer, and (c) iron oxide–iron nanocomposite stripes on an Au/Cr underlayer with different nominal sputtered Fe layer thickness ($d_{\text{Fe,nom}}$), all in comparison to the MR of the Au/Cr/SiO$_2$/Si substrate (gray line). (d) Schemes for the expected Fe$_3$O$_4$/Fe nanocomposite films (top) and MR at $\mu_0 H = 3$ T extracted from (c) in dependence of the nominal Fe thickness (bottom). A positive MR at the small thickness and a crossover to a negative MR at larger Fe thickness is observed. The dashed and dotted lines are guides to the eye.

several reports on positive MR effects in Fe$_3$O$_4$-based systems such as Fe$_3$O$_4$ nanowires,[50] thin films,[51] nanocomposites,[52,53] and heterojunctions.[54] To explain the positive MR effects in such Fe$_3$O$_4$-based devices, different mechanisms are proposed. The works of Liao et al.[50] and Reddy et al.[54] describe a spin-dependent scattering at the interface between the metal contact and the strongly spin-polarized magnetite, leading to a spin filter effect associated with high contact resistance. In the present study, such a contact effect is excluded because the native oxide layer was removed by Ar plasma etching prior to the sputter deposition of the Au contacts. In addition, the contact effect could not explain the distinct thickness dependence in our case.

Another mechanism is discussed for Fe$_3$O$_4$–Ag composites.[53,55] In these studies,[53,55] the positive MR effect is attributed to spin injection from the highly spin-polarized magnetite into diamagnetic Ag grains with zero spin polarization, and associated spin-dependent scattering at Fe$_3$O$_4$/Ag grain boundaries. This effect is only observed for a small compositional range, and a crossover to negative MR occurs for smaller and larger Ag amounts. We propose that in the present Fe$_3$O$_4$–Fe nanocomposite system, a similar effect causes the positive MR which is discussed in more detail in the following text.

At small thicknesses, granular film growth takes place and results in the presence of more or less coalesced iron nanoislands. Since these iron nanoislands are exposed to ambient conditions, their surface is completely oxidized. This is analogue to iron nanoparticles, which, after native oxidation at room temperature, yield iron cores covered by a Fe$_3$O$_4$ shell.[29,56] Thus, at small enough iron film thickness, the

volume of the oxidized regions after native oxidation will dominate over or be in the same order of magnitude of the volume of the iron grains. Thus, these films consist of a Fe$_3$O$_4$/Fe nanocomposite region, in which small Fe grains are distributed in the natural magnetite oxide layer, and a continuous Fe$_3$O$_4$ top layer (see scheme in Figure 3d). The top Fe$_3$O$_4$ layer is expected to give a negative contribution to MR. In the nanocomposite region, however, spin injection and spin reorientation can occur at the Fe$_3$O$_4$/Fe grain interfaces, similar to the case of Fe$_3$O$_4$/Ag nanocomposites,[53,55] since ferromagnetic Fe exhibits a lower spin polarization than Fe$_3$O$_4$. The increase in positive MR when increasing the thickness from 5 to 30 nm could then be caused by the increasing Fe$_3$O$_4$/Fe nanocomposite layer thickness, and associated increasing Fe$_3$O$_4$/Fe interface area, while the Fe$_3$O$_4$ top layer thickness remains constant (see scheme in Figure 3d). For small enough iron thickness, spin injection from Fe$_3$O$_4$ into the underlying Au will also occur, which even more resembles the Fe$_3$O$_4$–Ag system[53,55] because Au, like Ag, is a strong diamagnet. For the present iron oxide–iron nanocomposites, we measured a positive MR also on a (paramagnetic) Pd underlayer (see Supporting Information S3) and without a metal underlayer (Figure 3b). This indicates that interface scattering and spin injection from highly spin-polarized Fe$_3$O$_4$ in any metal with lower spin polarization, such as Ag,[53,55] or, in the present case Au, Pd, and Fe, can give rise to positive MR. The effect seems to be less pronounced on Pd compared to Au (see Supporting Information S3), but since the impact of interface scattering on the measured MR also strongly depends on the share of the electric current flowing through the different layers (and thus on the different resistivities), the origin for such differences in the magnitude of the positive MR cannot be resolved unambiguously at this point.
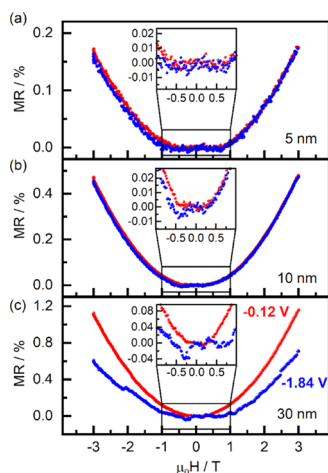
For the iron oxide–iron nanocomposites on Au (Figure 3c,d), the crossover to negative magnetoresistance, when $d_{\text{Fe,nom}}$ is increased to 40 nm, can be explained by the decreasing importance of interface effects, when more electric current flows through the (thicker) iron layer. Then, the negative magnetoresistance in iron will dominate the interface scattering and suppress the spin injection and the associated positive MR.

At $d_{\text{Fe,nom}} > 40$ nm, the magnitude of the MR remains similar. This signifies that no finite-size effects, which are sometimes reported for MR in iron thin films,[43] occur. Granberg et al.[43] showed that the electron mean free path in single-crystalline iron films at 300 K is in the order of 3 nm due to electron–phonon scattering. In the present iron oxide/iron films, the grain size is much larger than 3 nm, which consistently explains the thickness independent negative MR for samples thicker than 40 nm.

To achieve voltage control of MR by magneto-ionic reactions we applied electrolytic gating to selected Fe$_3$O$_4$/Fe stripe samples. Magneto-ionic control in metal oxide/metal films relies on oxidation/reduction processes, which can change the oxide/metal proportion.[25,32,57] Therefore, the strong dependency of the magnitude and sign of MR on $d_{\text{Fe,nom}}$ (and thus on the oxide/metal proportion) that we observed is highly promising for magneto-ionic control of MR. To investigate the possibility of magneto-ionic control, we chose nanocomposites with $d_{\text{Fe,nom}}$ equal to 5, 10, and 30 nm. These are samples with positive MR and, for the 30 nm sample, close to the crossover to negative MR. For the 40 nm sample, no MR change upon magneto-ionic reduction, i.e.,

voltage-induced iron layer thickness increase,[25] is expected, which is confirmed experimentally for the low field region (see Supporting Information S4).

As an electrolyte, we used 1 mol/L aqueous LiOH solution, which was added into the *in situ* transport cell. Different gate voltages were applied via a Pt counter electrode, and simultaneously the *in situ* MR measurements were conducted via press contacts outside the electrolyte area. Figure 4 shows

Figure 4. Voltage control of the magnitude and sign of MR by electrolytic gating. MR of iron oxide–iron nanocomposite stripes with $d_{Fe,nom}$ of (a) 5 nm, (b) 10 nm, and (c) 30 nm measured *in situ* during the polarization in LiOH solution at $E_{Red} = -1.84$ V (blue symbols) and $E_{Ox} = -0.12$ V (red symbols). The insets show the enlargement of the low magnetic field (± 1 T) region.

the MR signals for $d_{Fe,nom}$ = 5, 10, and 30 nm during the application of an oxidation potential (E_{Ox} = −0.12 V) or reduction potential (E_{Red} = −1.84 V). The MR curves with $d_{Fe,nom}$ of 5 and 10 nm (Figure 4a,b, respectively) show just minimal differences for the two gating voltages. This can be explained by the relatively thick Fe_3O_4 grain boundary layer, which is expected as the starting state (see scheme in Figure 3d). Possibly, in this case, the oxide in the grain boundaries cannot be reduced completely and, in consequence, residual oxide in the grain boundaries may prevent a change in the conduction mechanism. In contrast, a large voltage-induced change in MR is observed for the sample with $d_{Fe,nom}$ = 30 nm (Figure 4c). At the oxidation potential, a significantly larger positive MR effect is observed in comparison to the state at the reduction potential. At 3 T, the MR was reduced by about 0.5% upon reduction, corresponding to a relative change of −45%. The negative MR of ferromagnetic iron seems to play a more pronounced role during reduction, even though the positive MR attributed to spin injection in the nanocomposite region is still dominant. In the low-magnetic-field region between ±1 T (insets in Figure 4), signatures for the negative MR induced by E_{Red} appear in all three samples. These signatures occur between ±0.5 T and are more pronounced in the 10 and 30 nm samples. Thus, depending on the external magnetic field and the applied voltage, the MR can be set on and off and change its sign. For the 30 nm sample, the reversibility of the voltage-induced MR switching is demonstrated for two cycles (see Supporting Information S5). Reversibility of more than several hundred cycles may be expected, as this has been shown for oxidation/reduction in similar FeO_x/Fe nanostructure/alkaline electrolyte systems for

supercapacitor applications.[58] These findings show that, with our mechanism, a voltage-controlled sign change of MR can be achieved in low magnetic fields at room temperature. By further tuning the starting iron layer thickness close to the MR crossover (Figure 3d), the voltage-switching between positive and negative MR should be within reach also in the high-magnetic-field region.

■ CONCLUSIONS

The presented tunable MR relies on the combination of a spin-polarized Fe_3O_4 phase with nanocrystalline iron grains. So far, the introduction of artificial defects, such as vertical grain boundaries in perovskite manganite thin films[59] and crystalline boundaries in graphene,[60] was applied to tune MR in an irreversible manner. In contrast, in the present approach, the locally oxidized regions adjacent to iron are susceptible to voltage-induced reduction processes during electrolytic gating, which enables voltage-tunable MR. This represents an original route to a reversible control of MR on the base of magneto-ionic reactions. Since locally oxidized regions are the active tuning elements, the downscaling to nanometer-sized devices, with the limit of, *e.g.*, one oxidized grain boundary/device, might be within reach. Also, a transfer to solid electrolytes with similar redox behavior may be possible.[19] The large range of positive and negative MR values set by the thickness and a low voltage (∼1 V) at room temperature goes beyond state-of-the-art voltage-tunable MR devices, which are restricted to positive or negative MR,[11,16,17] high applied voltage,[15,17] or low-temperature operation.[12,15,61]

In summary, we investigated the MR of iron oxide–iron nanocomposite films for nominal sputtered iron thicknesses $d_{Fe,nom}$ from 5 to 50 nm. We found a rather unusual positive MR, which is attributed to surface and grain boundary oxidation causing spin injection and spin reorientation at the Fe_3O_4/Fe interfaces. The MR can be tuned by varying the deposited iron layer thickness and via voltage-gating in the alkaline electrolyte at room temperature. We recorded MR values from −0.11% for $d_{Fe,nom}$ = 50 nm up to +1.11% at 3 T for $d_{Fe,nom}$ = 30 nm. By applying gate voltages, a relative MR (3 T) change of 45% can be achieved by magneto-ionic switching between reduced and oxidized state. In the low-magnetic-field region, on/off switching and a sign change of MR can be achieved with a potential difference of only 1.72 V. The present approach signifies a step forward to practical and tunable room-temperature MR-based nanodevices, which can boost the development of nanoscale and energy-efficient magnetic field sensors with high sensitivity, magnetic memories, and magnetoelectric devices in general.

■ ASSOCIATED CONTENT

Ⓢ Supporting Information

The Supporting Information is available free of charge at https://pubs.acs.org/doi/10.1021/acsaelm.0c00448.

Raman spectroscopy to distinguish iron oxides; X-ray diffraction; effect of the type of underlayer on the MR of iron oxide–iron nanocomposite stripes; voltage control of iron oxide–iron nanocomposite stripe with $d_{Fe,nom}$= 40 nm; and reversibility of the MR switching by oxidation/reduction (PDF)

■ AUTHOR INFORMATION

Corresponding Author

Karin Leistner − *Leibniz IFW Dresden, 01069 Dresden, Germany; Institute of Material Science, Technische Universität Dresden, 01062 Dresden, Germany;* ⊙ orcid.org/0000-0002-8049-4877; Email: k.leistner@ifw-dresden.de

Authors

Martin Nichterwitz − *Leibniz IFW Dresden, 01069 Dresden, Germany; Physical Chemistry, Technische Universität Dresden, 01062 Dresden, Germany*

Shashank Honnali − *Leibniz IFW Dresden, 01069 Dresden, Germany*

Jonas Zehner − *Leibniz IFW Dresden, 01069 Dresden, Germany; Institute of Material Science, Technische Universität Dresden, 01062 Dresden, Germany*

Sebastian Schneider − *Leibniz IFW Dresden, 01069 Dresden, Germany; Dresden Center for Nanoanalysis (DCN), Center for Advancing Electronics Dresden (cfaed), TU Dresden, 01062 Dresden, Germany*

Darius Pohl − *Dresden Center for Nanoanalysis (DCN), Center for Advancing Electronics Dresden (cfaed), TU Dresden, 01062 Dresden, Germany*

Sandra Schiemenz − *Leibniz IFW Dresden, 01069 Dresden, Germany*

Sebastian T. B. Goennenwein − *Institut für Festkörper- und Materialphysik, Technische Universität Dresden, 01062 Dresden, Germany*

Kornelius Nielsch − *Leibniz IFW Dresden, 01069 Dresden, Germany; Institute of Material Science, Technische Universität Dresden, 01062 Dresden, Germany*

Complete contact information is available at:
https://pubs.acs.org/10.1021/acsaelm.0c00448

■ REFERENCES

(1) Valadeiro, J.; Cardoso, S.; Macedo, R.; Guedes, A.; Gaspar, J.; Freitas, P. Hybrid Integration of Magnetoresistive Sensors with MEMS as a Strategy to Detect Ultra-Low Magnetic Fields. *Micromachines* **2016**, *7*, 88.

(2) Freitas, P. P.; Ferreira, R.; Cardoso, S.; Cardoso, F. Magneto-resistive Sensors. *J. Phys.: Condens. Matter* **2007**, *19*, No. 165221.

(3) Nakatani, T.; Gao, Z.; Hono, K. Read Sensor Technology for Ultrahigh Density Magnetic Recording. *MRS Bull.* **2018**, *43*, 106−111.

(4) Chappert, C.; Fert, A.; Van Dau, F. N. The Emergence of Spin Electronics in Data Storage. *Nat. Mater.* **2007**, *6*, 813−823.

(5) Kent, A. D.; Worledge, D. C. A New Spin on Magnetic Memories. *Nat. Nanotechnol.* **2015**, *10*, 187−191.

(6) Lin, G.; Makarov, D.; Schmidt, O. G. Magnetic Sensing Platform Technologies for Biomedical Applications. *Lab Chip* **2017**, *17*, 1884−1912.

(7) Luo, Z.; Lu, Z.; Xiong, C.; Zhu, T.; Wu, W.; Zhang, Q.; Wu, H.; Zhang, X.; Zhang, X. Reconfigurable Magnetic Logic Combined with Nonvolatile Memory Writing. *Adv. Mater.* **2017**, *29*, No. 1605027.

(8) Deac, A. M.; Fukushima, A.; Kubota, H.; Maehara, H.; Suzuki, Y.; Yuasa, S.; Nagamine, Y.; Tsunekawa, K.; Djayaprawira, D. D.; Watanabe, N. Bias-Driven High-Power Microwave Emission from MgO-Based Tunnel Magnetoresistance Devices. *Nat. Phys.* **2008**, *4*, 803−809.

(9) Matsukura, F.; Tokura, Y.; Ohno, H. Control of Magnetism by Electric Fields. *Nat. Nanotechnol.* **2015**, *10*, 209−220.

(10) Liu, P.; Lin, X.; Xu, Y.; Zhang, B.; Si, Z.; Cao, K.; Wei, J.; Zhao, W. Optically Tunable Magnetoresistance Effect: From Mechanism to Novel Device Application. *Materials* **2018**, *11*, No. 47.

(11) Li, S.; Luo, W.; Gu, J.; Cheng, X.; Ye, P. D.; Wu, Y. Large, Tunable Magnetoresistance in Nonmagnetic III−V Nanowires. *Nano Lett.* **2015**, *15*, 8026−8031.

(12) Zhang, Y.; Fan, J.; Huang, Q.; Zhu, J.; Zhao, Y.; Li, M.; Wu, Y.; Huang, R. Voltage-Controlled Magnetoresistance in Silicon Nanowire Transistors. *Sci. Rep.* **2018**, *8*, No. 15194.

(13) Zwanenburg, F. A.; van der Mast, D. W.; Heersche, H. B.; Kouwenhoven, L. P.; Bakkers, E. P. A. M. Electric Field Control of Magnetoresistance in InP Nanowires with Ferromagnetic Contacts. *Nano Lett.* **2009**, *9*, 2704−2709.

(14) Oltscher, M.; Eberle, F.; Kuczmik, T.; Bayer, A.; Schuh, D.; Bougeard, D.; Ciorga, M.; Weiss, D. Gate-Tunable Large Magneto-resistance in an All-Semiconductor Spin Valve Device. *Nat. Commun.* **2017**, *8*, No. 1807.

(15) Zhang, E.; Chen, R.; Huang, C.; Yu, J.; Zhang, K.; Wang, W.; Liu, S.; Ling, J.; Wan, X.; Lu, H.-Z.; Xiu, F. Tunable Positive to Negative Magnetoresistance in Atomically Thin WTe_2. *Nano Lett.* **2017**, *17*, 878−885.

(16) Skowroński, W.; Wiśniowski, P.; Stobiecki, T.; Cardoso, S.; Freitas, P. P.; van Dijken, S. Magnetic Field Sensor with Voltage-Tunable Sensing Properties. *Appl. Phys. Lett.* **2012**, *101*, No. 192401.

(17) Wang, L.; Hu, Z.; Zhu, Y.; Xian, D.; Cai, J.; Guan, M.; Wang, C.; Duan, J.; Wu, J.; Wang, Z.; Zhou, Z.; Jiang, Z.-D.; Zeng, Z.; Liu, M. Electric Field-Tunable Giant Magnetoresistance (GMR) Sensor with Enhanced Linear Range. *ACS Appl. Mater. Interfaces* **2020**, *12*, 8855−8861.

(18) Leistner, K.; Wunderwald, J.; Lange, N.; Oswald, S.; Richter, M.; Zhang, H.; Schultz, L.; Fähler, S. Electric-Field Control of Magnetism by Reversible Surface Reduction and Oxidation Reactions. *Phys. Rev. B* **2013**, *87*, No. 224411.

(19) Bauer, U.; Yao, L.; Tan, A. J.; Agrawal, P.; Emori, S.; Tuller, H. L.; van Dijken, S.; Beach, G. S. D. Magneto-Ionic Control of Interfacial Magnetism. *Nat. Mater.* **2015**, *14*, 174−181.

(20) Molinari, A.; Hahn, H.; Kruk, R. Voltage-Control of Magnetism in All-Solid-State and Solid/Liquid Magnetoelectric Composites. *Adv. Mater.* **2019**, *31*, No. 1806662.

(21) Navarro-Senent, C.; Quintana, A.; Menéndez, E.; Pellicer, E.; Sort, J. Electrolyte-Gated Magnetoelectric Actuation: Phenomenology, Materials, Mechanisms, and Prospective Applications. *APL Mater.* **2019**, *7*, No. 030701.

(22) Duschek, K.; Petr, A.; Zehner, J.; Nielsch, K.; Leistner, K. All-Electrochemical Voltage-Control of Magnetization in Metal Oxide/Metal Nanoislands. *J. Mater. Chem. C* **2018**, *6*, 8411−8417.

(23) Quintana, A.; Menéndez, E.; Liedke, M. O.; Butterling, M.; Wagner, A.; Sireus, V.; Torruella, P.; Estradé, S.; Peiró, F.; Dendooven, J.; Detavernier, C.; Murray, P. D.; Gilbert, D. A.; Liu, K.; Pellicer, E.; Nogues, J.; Sort, J. Voltage-Controlled ON−OFF Ferromagnetism at Room Temperature in a Single Metal Oxide Film. *ACS Nano* **2018**, *12*, 10291−10300.

(24) Gilbert, D. A.; Olamit, J.; Dumas, R. K.; Kirby, B. J.; Grutter, A. J.; Maranville, B. B.; Arenholz, E.; Borchers, J. A.; Liu, K. Controllable

Positive Exchange Bias via Redox-Driven Oxygen Migration. *Nat. Commun.* **2016**, *7*, No. 11050.

(25) Zehner, J.; Huhnstock, R.; Oswald, S.; Wolff, U.; Soldatov, I.; Ehresmann, A.; Nielsch, K.; Holzinger, D.; Leistner, K. Nonvolatile Electric Control of Exchange Bias by a Redox Transformation of the Ferromagnetic Layer. *Adv. Electron. Mater.* **2019**, *5*, No. 1900296.

(26) Tsuchiya, T.; Terabe, K.; Ochi, M.; Higuchi, T.; Osada, M.; Yamashita, Y.; Ueda, S.; Aono, M. *In Situ* Tuning of Magnetization and Magnetoresistance in Fe_3O_4 Thin Film Achieved with All-Solid-State Redox Device. *ACS Nano* **2016**, *10*, 1655−1661.

(27) Graham, M. J.; Ali, S. I.; Cohen, M. Low Temperature Oxidation (24° to 200 °C) and Krypton Adsorption Studies on Polycrystalline and Single Crystal Iron Surfaces. *J. Electrochem. Soc.* **1970**, *117*, 513.

(28) Jiménez-Villacorta, F.; Muñoz-Martín, A.; Prieto, C. Study of Oxidized Iron Thin Films by Non-Rutherford Elastic Scattering. *Nucl. Instrum. Methods Phys. Res., Sect. B* **2006**, *249*, 486−489.

(29) Meng, S.; Wu, J.; Zhao, L.; Zheng, H.; Jia, S.; Hu, S.; Meng, W.; Pu, S.; Zhao, D.; Wang, J. Atomistic Insight into the Redox Reactions in Fe/Oxide Core−Shell Nanoparticles. *Chem. Mater.* **2018**, *30*, 7306−7312.

(30) Shebanova, O. N.; Lazor, P. Raman Study of Magnetite (Fe_3O_4): Laser-Induced Thermal Effects and Oxidation. *J. Raman Spectrosc.* **2003**, *34*, 845−852.

(31) Leistner, K.; Lange, N.; Hänisch, J.; Oswald, S.; Scheiba, F.; Fähler, S.; Schlörb, H.; Schultz, L. Electrode Processes and in Situ Magnetic Measurements of FePt Films in a $LiPF_6$ Based Electrolyte. *Electrochim. Acta* **2012**, *81*, 330−337.

(32) Duschek, K.; Pohl, D.; Fähler, S.; Nielsch, K.; Leistner, K. Research Update: Magnetoionic Control of Magnetization and Anisotropy in Layered Oxide/Metal Heterostructures. *APL Mater.* **2016**, *4*, No. 032301.

(33) Duschek, K.; Uhlemann, M.; Schlörb, H.; Nielsch, K.; Leistner, K. Electrochemical and in Situ Magnetic Study of Iron/Iron Oxide Films Oxidized and Reduced in KOH Solution for Magneto-Ionic Switching. *Electrochem. Commun.* **2016**, *72*, 153−156.

(34) Leistner, K.; Krause, A.; Fähler, S.; Schlörb, H.; Schultz, L. Electrode Processes during Fe−Pt Electrodeposition Studied by Electrochemical Quartz Crystal Microbalance. *Electrochim. Acta* **2006**, *52*, 170−176.

(35) Fleischer, K.; Mauit, O.; Shvets, I. V. Stability and Capping of Magnetite Ultra-Thin Films. *Appl. Phys. Lett.* **2014**, *104*, No. 192401.

(36) Jubb, A. M.; Allen, H. C. Vibrational Spectroscopic Characterization of Hematite, Maghemite, and Magnetite Thin Films Produced by Vapor Deposition. *ACS Appl. Mater. Interfaces* **2010**, *2*, 2804−2812.

(37) Schwaminger, S. P.; Bauer, D.; Fraga-García, P.; Wagner, F. E.; Berensmeier, S. Oxidation of Magnetite Nanoparticles: Impact on Surface and Crystal Properties. *CrystEngComm* **2017**, *19*, 246−255.

(38) Takeno, Y.; Iwama, Y. Structure and Magnetic Properties of Iron Films Deposited at Oblique Incidence. *J. Magn. Magn. Mater.* **1983**, *35*, 293−295.

(39) Lawless, K. R. The Oxidation of Metals. *Rep. Prog. Phys.* **1974**, *37*, 231−316.

(40) Kim, Y. K.; Oliveria, M. Magnetic Properties of Sputtered Fe Thin Films: Processing and Thickness Dependence. *J. Appl. Phys.* **1993**, *74*, 1233−1241.

(41) Cornell, R. M.; Schwertmann, U. *The Iron Oxides: Structure, Properties, Reactions, Occurrence, and Uses*; VCH: Weinheim; New York, 1996.

(42) Zhang, D. L.; Song, X. H.; Zhang, X.; Zhang, X.-G. Magnetoresistance of Au Films. *J. Appl. Phys.* **2014**, *116*, No. 223704.

(43) Granberg, P.; Isberg, P.; Baier, T.; Hjörvarsson, B.; Nordblad, P. Anisotropic Behaviour of the Magnetoresistance in Single Crystalline Iron Films. *J. Magn. Magn. Mater.* **1999**, *195*, 1−8.

(44) Stankiewicz, J.; Jiménez-Villacorta, F.; Prieto, C. Magnetotransport Properties of Oxidized Iron Thin Films. *Phys. Rev. B* **2006**, *73*, No. 014429.

(45) Felix, J. F.; Figueiredo, L. C.; Mendes, J. B. S.; Morais, P. C.; Araujo, C. I. L. de. Low-Field Microwave Absorption and Magnetoresistance in Iron Nanostructures Grown by Electrodeposition on n-Type Lightly Doped Silicon Substrates. *J. Magn. Magn. Mater.* **2015**, *395*, 130−133.

(46) Coey, J. M. D.; Berkowitz, A. E.; Balcells, L.; Putris, F. F.; Parker, F. T. Magnetoresistance of Magnetite. *Appl. Phys. Lett.* **1998**, *72*, 734−736.

(47) Liu, K.; Zhao, L.; Klavins, P.; Osterloh, F. E.; Hiramatsu, H. Extrinsic Magnetoresistance in Magnetite Nanoparticles. *J. Appl. Phys.* **2003**, *93*, 7951−7953.

(48) Ziese, M.; Höhne, R.; Semmelhack, H. C.; Reckentin, H.; Hong, N. H.; Esquinazi, P. Mechanism of Grain-Boundary Magnetoresistance in Fe O Films. *Eur. Phys. J. B* **2002**, *28*, 415−422.

(49) Park, C.; Peng, Y.; Zhu, J.-G.; Laughlin, D. E.; White, R. M. Magnetoresistance of Polycrystalline $Fe3O4$ Films Prepared by Reactive Sputtering at Room Temperature. *J. Appl. Phys.* **2005**, *97*, No. 10C303.

(50) Liao, Z.-M.; Li, Y.-D.; Xu, J.; Zhang, J.-M.; Xia, K.; Yu, D.-P. Spin-Filter Effect in Magnetite Nanowire. *Nano Lett.* **2006**, *6*, 1087−1091.

(51) Chopdekar, R. V.; Hu, G.; Ford, A. C.; Suzuki, Y. Magnetics and Magnetoresistance in Epitaxial Magnetite Heterostructures. *J. Electron. Mater.* **2004**, *33*, 1254−1258.

(52) Gu, H.; Huang, Y.; Zhang, X.; Wang, Q.; Zhu, J.; Shao, L.; Haldolaarachchige, N.; Young, D. P.; Wei, S.; Guo, Z. Magnetoresistive Polyaniline-Magnetite Nanocomposites with Negative Dielectric Properties. *Polymer* **2012**, *53*, 801−809.

(53) Hsu, J.-H.; Chen, S.-Y.; Chang, C.-R. Anomalous Positive Magnetoresistance in $Fe3O4$−Ag Composite Films. *J. Magn. Magn. Mater.* **2002**, *242−245*, 479−481.

(54) Reddy, K. M.; Padture, N. P.; Punnoose, A.; Hanna, C. Heterojunction Metal-Oxide-Metal Au-Fe_3O_4-Au Single Nanowire Device for Spintronics. *J. Appl. Phys.* **2015**, *117*, No. 17D710.

(55) Master, R.; Choudhary, R. J.; Phase, D. M. Effect of Silver Addition on Structural, Electrical and Magnetic Properties of Fe_3O_4 Thin Films Prepared by Pulsed Laser Deposition. *J. Appl. Phys.* **2012**, *111*, No. 073907.

(56) Leistner, K.; Yang, M.; Damm, C.; Oswald, S.; Petr, A.; Kataev, V.; Nielsch, K.; Kavanagh, K. L. Aligned Cuboid Iron Nanoparticles by Epitaxial Electrodeposition. *Nanoscale* **2017**, *9*, 5315−5322.

(57) Quintana, A.; Menéndez, E.; Isarain-Chávez, E.; Fornell, J.; Solsona, P.; Fauth, F.; Baró, M. D.; Nogués, J.; Pellicer, E.; Sort, J. Tunable Magnetism in Nanoporous CuNi Alloys by Reversible Voltage-Driven Element-Selective Redox Processes. *Small* **2018**, *14*, No. 1704396.

(58) Wang, H.; Liang, Y.; Gong, M.; Li, Y.; Chang, W.; Mefford, T.; Zhou, J.; Wang, J.; Regier, T.; Wei, F.; Dai, H. An Ultrafast Nickel−Iron Battery from Strongly Coupled Inorganic Nanoparticle/Nanocarbon Hybrid Materials. *Nat. Commun.* **2012**, *3*, No. 917.

(59) Chen, A.; Bi, Z.; Tsai, C.-F.; Lee, J.; Su, Q.; Zhang, X.; Jia, Q.; MacManus-Driscoll, J. L.; Wang, H. Tunable Low-Field Magnetoresistance in (La0.7Sr0.3MnO3)0.5:(ZnO)0.5 Self-Assembled Vertically Aligned Nanocomposite Thin Films. *Adv. Funct. Mater.* **2011**, *21*, 2423−2429.

(60) Rehman Sagar, R. U.; Shehzad, K.; Ali, A.; Stadler, F. J.; Khan, Q.; Zhao, J.; Wang, X.; Zhang, M. Defect-Induced, Temperature-Independent, Tunable Magnetoresistance of Partially Fluorinated Graphene Foam. *Carbon* **2019**, *143*, 179−188.

(61) Yang, W.; Shi, Q.; Miao, T.; Li, Q.; Cai, P.; Liu, H.; Lin, H.; Bai, Y.; Zhu, Y.; Yu, Y.; Deng, L.; Wang, W.; Yin, L.; Sun, D.; Zhang, X.-G.; Shen, J. Achieving Large and Nonvolatile Tunable Magnetoresistance in Organic Spin Valves Using Electronic Phase Separated Manganites. *Nat. Commun.* **2019**, *10*, No. 3877.